



**HAL**  
open science

## Experimental study of slotted hole bolted cover-plate connection using full field measurement

Evelyne Toussaint, Edouard Cavène, Sébastien Durif, Abdelhamid Bouchaïr

### ► To cite this version:

Evelyne Toussaint, Edouard Cavène, Sébastien Durif, Abdelhamid Bouchaïr. Experimental study of slotted hole bolted cover-plate connection using full field measurement. Structures, 2020, 23, pp.573-587. 10.1016/j.istruc.2019.09.003 . hal-03434676

**HAL Id: hal-03434676**

**<https://uca.hal.science/hal-03434676>**

Submitted on 21 Jul 2022

**HAL** is a multi-disciplinary open access archive for the deposit and dissemination of scientific research documents, whether they are published or not. The documents may come from teaching and research institutions in France or abroad, or from public or private research centers.

L'archive ouverte pluridisciplinaire **HAL**, est destinée au dépôt et à la diffusion de documents scientifiques de niveau recherche, publiés ou non, émanant des établissements d'enseignement et de recherche français ou étrangers, des laboratoires publics ou privés.



Distributed under a Creative Commons Attribution - NonCommercial 4.0 International License

## Experimental study of slotted hole bolted cover-plate connection using full field measurement

Edouard Cavène<sup>a</sup>, Sébastien Durif<sup>a</sup>, Abdelhamid Bouchair<sup>a</sup>, Evelyne Toussaint<sup>a,1</sup>,

<sup>a</sup>*Université Clermont Auvergne, CNRS, Institut Pascal, F-63000 Clermont-Ferrand, France*

---

### Abstract

This study investigates the ductile failure modes associated to bearing mode for bolted cover-plates with slotted holes on the basis of an experimental program. The strengths from tests are compared to those given by two analytical models based on design standards. Two tested specimens were monitored to observe the local deformations of the loaded zones at the end-distance of the plates. The deformations are measured using Digital Image Correlation (DIC) technique. Strain maps showed that the behavior of the plates with slotted-holes is very complex combining, in some cases, bending, shear and tension of the loaded part under the bolt. The wealth of information leads to a better understanding of the behavior of slotted hole connections until failure and proposes an analysis on the limits of the existing analytical approaches.

*Keywords:* Experimental tests, cover-plate joints, slotted holes, Eurocode 3, DIC

---

---

<sup>1</sup>evelyne.toussaint@uca.fr

## 1. Introduction

In steel construction, cover-plate connections play an important role in the mechanical behavior of structures. Those connections are mostly submitted to shearing [1]. Shearing connections modeled as cover-plates present the advantage to realize a large number of connection types (beam-to-beam, beam-to-column or column-to-column connection) with a limited bulkiness in comparison with that of end-plate connections modeled as T-stubs [2, 3]. Cover-plate joints with circular holes allow to transfer bending using the shearing of the bolt and tension with local shearing of the plate [4]. With this type of loading, various failure modes such as bearing, net-section or shearing of the bolt can occur [5]. In practice, ductile failure modes have to be privileged in the design of structures [6]. In that purpose, the bearing failure mode is the one to be considered in the design of structures. Some parameters influence this failure mode such as the geometry (end-distance and edge distance) [7]. The behavior of such connection is studied in various scientific papers [4, 8, 9]. To analyze the behavior of such connections, full-field measurement technique can be used to analyze in details strain fields in terms of mechanism of deformation [10].

Nowadays, the architectural tendencies combine different materials in the structures. Thus, connections between timber and steel [11] are common. In this context, new structural conditions are taken up regarding the material behavior, such as the brittle character of wood in tension perpendicular to grain or shear, mainly due to changing environment parameters such as temperature or moisture. One solution consists in giving additional degrees of freedom in order to limit the effect of the deformation gradients between the connected materials (steel and timber, for instance), or to improve the ductility and energy dissipation of connections in earthquake environment

[12, 13]. In order to release a degree of freedom, bolted cover-plates with slotted holes can also be used as a solution in the design of connections between different materials [14]. However, very few studies deal with this type of connection under loading perpendicular to the length of the hole. Two analytical models used to predict the bearing strength of such connections are available in the literature [15, 16, 17].

In the present study, the strength values given by the two models are compared to those obtained from experimental tests in order to evaluate the accuracy of the models and their limits of applications. Then, the non-linear load-displacement curves are observed at different stages of loading in order to describe the behavior of cover-plate with slotted holes. Besides, the DIC technique is used to analyze in details the local behavior of two specific geometries. Those local measurements aim at understanding the different mechanisms of deformation under the bolt for different load values observed on the load-displacement curve.

## **2. Geometry of the specimens**

This study aims at analyzing the behavior of bolted cover-plates with slotted holes considering the bearing failure mode. For that purpose, the edge distance is chosen to avoid net-section failure.

The experimental program concerns 14 specimens, with various hole lengths and end-distances, tested until failure. In a first time, twelve specimens are tested for the global analysis based on load-displacement curves. Then, to analyze the evolution of the strain distribution under the bolts, two specimens presenting different failure modes are equipped to perform DIC (Digital Image Correlation) measurement.

Figure 1 gives the geometrical parameters of a slotted hole using the

terms of Eurocode 3.

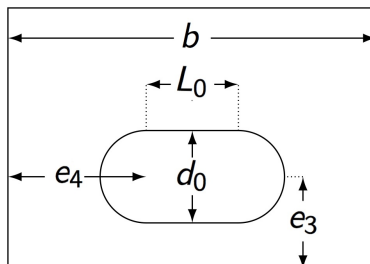


Figure 1: Geometrical characteristics of a slotted hole

The European standard defines minimum values for the distance from the axis of a slotted hole to the adjacent end or edge of any part ( $e_3$ ) and the distance from the centre of the end radius of a slotted hole to the adjacent end or edge of any part ( $e_4$ ) (see Table 1).

Parameter	Minimum value
$e_3$	$1.5 d_0$
$e_4$	$1.5 d_0$

Table 1: Geometrical recommendations of the Eurocode for slotted hole

In order to understand the mechanical behavior of the slotted holes with various geometrical configurations, some specimens are chosen with end-distances values out of the geometrical recommendations of NF-EN-1993-1-8 [18]. Among the six geometrical configurations tested, two are chosen with the end-distance ( $e_3$ ) lower than the minimum value given by Eurocode 3 [18]. The geometries with dimension lower than the one of the Eurocode 3 standard are chosen in order to maximize the effect of bending of the end-distance zone under the bolt. The dimensions of the six configurations are chosen so as to exclude bolt shear and net cross-section failure modes.

The geometrical characteristics of the tested cover-plate specimens are given in Table 2. Each configuration of specimens is tested twice. Thus, twelve specimens are tested in the analysis of the global behavior. The bolt is loaded in double shear to obtain a symmetrical set-up on the testing machine (see Figure 11). The end-distances of the specimens E1-1 and E2-1 are chosen with end-distance values under the limits defined by EN-1993-1-8.

Specimen	$L_0$ (mm)	$e_3$ (mm)	$e_4$ (mm)	$d_0$ (mm)	b (mm)	t (mm)
E1-1*	13	13	26	13	65	6
E1-1.5*		19,5				
E1-2		26				
E2-1	26	13	26	13	78	6
E2-1.5		19,5				
E2-2		26				
* : Specimens equipped with DIC						

Table 2: Geometrical characteristics of the tested specimens

The name of each specimen is chosen to take into account the analyzed parameters which are the length and the end distance. Thus, Ei-j corresponds to a configuration with slotted hole length of  $L_0 = i \cdot d_0$  and end-distance of  $e_3 = j \cdot d_0$ . As illustration, the specimen E1-1.5 is characterized by a hole length ( $L_0$ ) equal to  $1d_0$  and an end-distance ( $e_3$ ) equal to  $1.5d_0$ .

### 3. Global analysis : experimental tests and evaluation of existing models

The aim of this section is to evaluate the analytical model on a panel of experimentally tested geometries. First of all, the analytical models are applied to the tested geometries and compared to experimental results.

### 3.1. Tests set-up and material specifications

All specimens were tested using a  $\pm 200$  kN Zwick testing machine. The displacement controlled tensile tests were realized with a displacement rate of the cross-head machine chosen equal to  $0.04$  mm/s. The tests were performed in-order-to characterize the global behavior of the cover-plate connections. The load-displacement curves are obtained by the sensors of the testing machine.

The specimens have been made using a plate of S275 grade with a real value of yield strength of 290 MPa and an ultimate strength of 380 MPa. These mean values have been obtained by tensile tests on three coupon specimens. A sample of a stress-strain curve is presented in Figure 2.

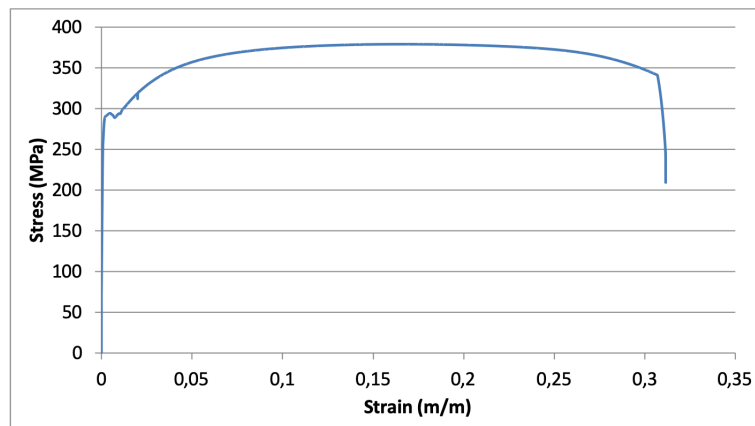


Figure 2: Example of a stress-strain curve of coupon tests

M12 bolts with grade 8.8 are used. The aim is to avoid the failure mode of bolts in shear as the study is focused on the bearing failure mode of the connected plates. To obtain the real characteristics of the bolts, tests in tension were performed. The real value of bolts tensile strength is equal to  $846$  MPa.

### 3.2. Design analytical models

This section describes two analytical models dealing with the bearing design strength of bolted cover-plate joints with slotted holes. The first one, proposed by Wald et al [15, 16], allows the strength prediction of cover-plate with slotted holes. It is similar to that used in the current version of Eurocode 3 [18]. The second one is developed by Moze for the draft of the coming version of Eurocode 3 [17]. The design equations are used as analytical formulas with the partial safety factor  $\gamma_{Mb}$  taken equal to 1.0. The obtained strength values with both models are compared to the plastic load capacity deduced from the experimental load-displacement curves. These curves present a bi-linear shape, the plastic strength corresponds to the slope changing. These two models are proposed with the geometrical limitations of the Eurocode 3 for cover-plate with slotted-holes which are an end-distance and edge-distance higher than  $1.5 d_0$  ( $e_3 \geq 1.5 d_0$  and  $e_4 \geq 1.5 d_0$ ). For E1-1 and E2-1, the end-distance is lower than the standard recommendations in order to maximize the effect of bending.

The following notations are used:  $d$  is the bolt diameter,  $d_0$  is the diameter of the hole,  $t$  is the plate thickness,  $f_u$  and  $f_{ub}$  are the ultimate tensile strength of the plate and the bolt, respectively.

The framework of the study is presented so the analytical models are now presented.

#### 3.2.1. Bearing model of Wald [15]

According to the model of Wald, the bearing strength ( $F_{b,Rd}$ ) is evaluated using Equation 1.

$$F_{b,Rd,Wald} = \beta \cdot \frac{2.5 \cdot \alpha \cdot f_u \cdot d \cdot t}{\gamma_{Mb}} \quad (1)$$

with

$$\alpha = \min \left( \frac{e_3}{3d_0}; \frac{f_{ub}}{f_u}; 1 \right)$$

The coefficient  $\beta$  in Equation 1 is the reduction factor of the circular hole strength in bearing allowing to obtain that of slotted hole. It has been calibrated using a statistical analysis based on experimental results. The analysis gives different values of  $\beta$  depending on the hole length. For short slotted holes ( $d+2 \text{ mm} \leq L_0+d_0 \leq d+6 \text{ mm}$ ), a value of 0.9 for  $\beta$  is efficient and for long slotted holes ( $d+6 \text{ mm} \leq L_0+d_0 \leq 2.5d$ ), a value of 0.7 for  $\beta$  is the most appropriate solution. Authors conclude that a value of 0.6 for  $\beta$  gives good results for very long slotted holes ( $2.5d \leq L_0+d_0 \leq 3.5d$ ). In order to propose a design rule for all slotted holes despite their length, the coefficient value of  $\beta$  equal to 0.6 is chosen by the authors and used in the Eurocode 3 standard in order to evaluate the bearing strength of slotted holes. Another study [19] confirmed this reduction factor choice. Indeed, this study compares the bearing strength of plates with two circular holes in serie connected to plates with two circular holes or one circular hole and one slotted in serie. A decrease of 40% of the strength capacity was observed for the configuration with the slotted hole in comparison with that with circular hole.

Table 3 summarizes the strength values corresponding to the bearing failure mode for all the specimens using the mechanical characteristics of Table 3 and a safety factor  $\gamma_{Mb}$  taken equal to 1.

The model of Wald et al [15] is based on a small deformations criterion of the end-distance. For this reason, the values given by this model are compared with the plastic values taken from the experimental load-displacement curves in section 3.3.

Specimen	$F_{b,Rd,Wald}$
E1-1	13.7
E1-1.5	20.5
E1-2	27.4
E2-1	13.7
E2-1.5	20.5
E2-2	27.4

Table 3: Strengths of the bearing failure mode in  $kN$  according to the model of Wald

### 3.2.2. Bearing model of Moze [17]

This model presented in the draft of the Eurocode [17] has two main specificities. Firstly, it takes into account the length of the hole in the reduction factor applied to the bearing strength of a circular hole. The second one consists in choosing, as resistance criterion for the slotted hole, the load corresponding to the hole elongation obtained from the maximum load for the corresponding circular hole. This model is obtained on the basis of numerical tests.

The experimental strength, named  $F(u_{s,max})$ , is defined using the load-displacement curve of a plate with circular hole presenting the same mechanical and geometrical parameters as the one tested with slotted holes. On this curve,  $u_{s,max}$  is the displacement corresponding to the maximum load of the circular hole. A good estimation of the  $u_{s,max}$  value is  $\frac{e_3}{3}$  for circular holes. This deflection value is reported on the load-displacement curve for the connection with slotted hole in order to obtain its design strength.

The design model of Moze takes into-account the large deformation capacities of such connections before failure. It can be used to design connections where large deformation is allowed. The design model proposed by Moze is presented in equation 2.

$$F_{b,Rd,Moze} = k_b \frac{k_1 \cdot f_u \cdot d \cdot t}{\gamma_{M2}} \quad (2)$$

with,

$$k_1 = \min \left( \frac{e_3}{d_0}; 3 \right) \quad (3)$$

and

$$k_b = 0.9 ; \text{ for } d + 2 \text{ mm} \leq L_0 \leq d + 6 \text{ mm} \quad (4)$$

$$k_b = \min(0.375 \cdot k_1 + 0.15; 0.9) ; \text{ for } d + 6 \text{ mm} \leq L_0 \leq 2.5d \quad (5)$$

$$k_b = \min(0.375 \cdot k_1; 0.9) ; \text{ for } 2.5d \leq L_0 \leq 3.5d \quad (6)$$

$d$  is the bolt diameter,  $d_0$  is the diameter of the hole,  $t$  is the plate thickness,  $f_u$  and  $f_{ub}$  are the ultimate tensile strength of the plate and the bolt respectively. This method has been applied on the tested configurations and the values of  $k_b$  and  $F_{b,Rd,Moze}$  are presented in Table 4.

Specimen	Bearing strength	
	$k_b$	$F_{b,Rd,Moze}$
E1-1	0.9	24.6
E1-1.5	0.9	36.9
E1-2	0.9	49.2
E2-1	0.525	14.4
E2-1.5	0.7125	29.2
E2-2	0.9	49.2

Table 4: Bearing failure mode strengths in  $kN$  according to the model of Moze

In conclusion, based on the criterion of deformation considered for the presented models, the model of Wald et al can be used as design rule for small deformation of the end-distance while the model of Moze allows large deformations. Moreover, in order to evaluate the accuracy of both models,

their strength values are compared to those obtained from experimental tests in section 3.3.

### 3.3. Experimental results and comparison with analytical models

Experimental tests were performed until failure of the connection, except for E2-2 specimen for which an out of plane bending of the plate was observed during the test due to the bending of the bolt (see Figure 4). However, the load-displacement curve reached large deformations in plastic stage and it can be analyzed similarly to the other specimens. Global load-displacement curves are presented in Figure 3, where two specimens are tested for each geometry.

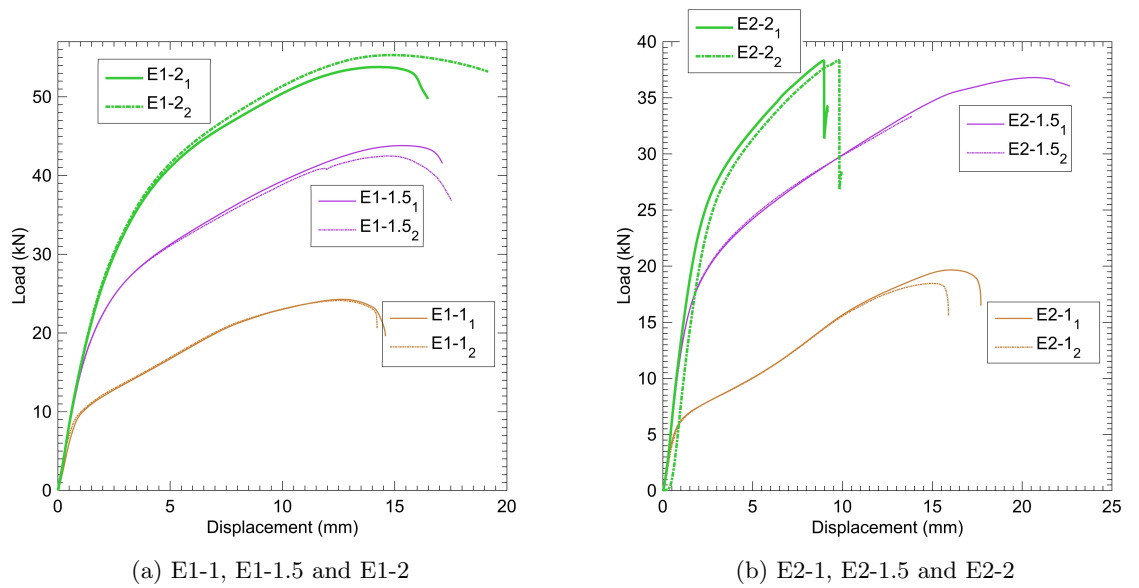


Figure 3: Load-displacement curves

Load-displacement curves can be represented by a bi-linear law, see [16]. However, regarding the shape of experimental curves, instead of defining the second stiffness as the initial one divided by ten, the second stiffness is defined using linear regression. In the study, three load values are defined to



Figure 4: Out of plane bending of E2-2

characterize the global behavior of such connections. The first value, named plastic strength ( $F_{pl}$ ), corresponds to the changing of the curve slope. The second value  $F(u_{s,max})$  is the load value corresponding to the displacement  $u_{s,max} = \frac{e_3}{3}$  according to the model of Moze. The last one is the ultimate load ( $F_{ult}$ ) defined as the maximum load reached before failure. The three loads  $F_{pl}$ ,  $F(u_{s,max})$  and  $F_{ult}$  are presented in Figure 5 for a typical load-displacement curve.

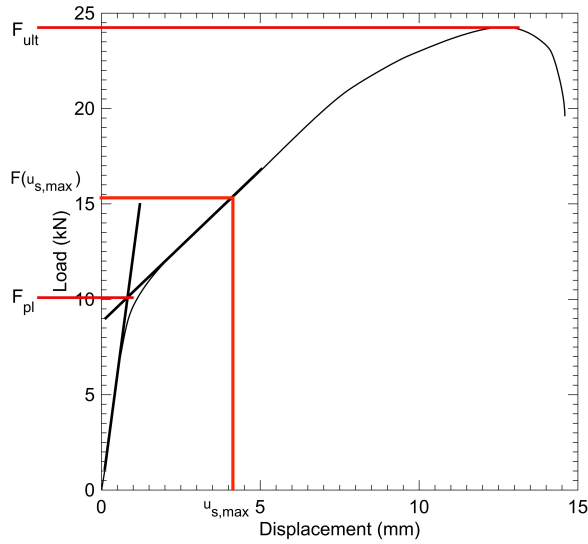


Figure 5: Definition of  $F_{pl}$ ,  $F(u_{s,max})$  and  $F_{ult}$

$F_{pl}$  values are taken as the reference strength values to be compared with

the design values obtained using the bearing strength of the Wald model  $F_{b,Rd,Wald}$ . The  $F(u_{s,max})$  values are compared to the bearing strength values obtained from the model of Moze  $F_{b,Rd,Moze}$ . Relative differences named  $e_{Wald}$  and  $e_{Moze}$  between  $F_{pl}$  and  $F_{b,Rd,Wald}$  and  $F(u_{s,max})$  and  $F_{b,Rd,Moze}$  are defined in Equations 7 and 8. The geometrical recommendations of these models are reminded in Table 5.

$$e_{Wald} = \frac{F_{pl} - F_{b,Rd,Wald}}{F_{pl}} \cdot 100 \text{ [\%]} \quad (7)$$

$$e_{Moze} = \frac{F(u_{s,max}) - F_{b,Rd,Moze}}{F(u_{s,max})} \cdot 100 \text{ [\%]} \quad (8)$$

Parameter	Minimum value
$e_3$	$1.5 d_0$
$e_4$	$1.5 d_0$

Table 5: Geometrical recommendations of the Eurocode for slotted hole

Results are presented in Table 6 and 7.

Specimen	$F_{pl}$ (kN)	$F_{b,Rd,Wald}$ (kN)	Difference ( $e_{Wald}$ in %)	$F_{ult}$
E1-1	10.2	13.7	-34	24
E1-1.5	27	20.5	24	43
E1-2	38	27.4	28	55
E2-1	6.5	13.7	-111	19
E2-1.5	21.5	20.5	5	37
E2-2	26.5	27.4	-3	38

Table 6: Comparison between experimental values and design model of Wald

Regarding the specimens E2-1.5 and E2-2, it can be observed that strength values  $F_{b,Rd,Wald}$  are very close to the experimental plastic values  $F_{pl}$ . A higher difference is observed between Wald model and tests for specimens

Specimen	$u_{s,max}$	$F(u_{s,max})$	$F_{b,Rd,Moze}$ ( $kN$ )	Difference ( $e_{Moze}$ in %)	$F_{ult}$
E1-1	4.3	15.6	24.6	-58	24
E1-1.5	6.5	37.4	37	1	43
E1-2	8.7	53.2	49.2	7.5	55
E2-1	4.3	9.5	14.4	-52	19
E2-1.5	6.5	26.3	29.2	-11	37
E2-2	8.7	38	49.2	-29	38

Table 7: Comparison between experimental values and design model of Moze

E1-1.5 and E1-2 (about 25%). Indeed, the analytical model does not take into account the length of the hole and in accordance with the development of the model [15], it seems more adapted for long slotted holes. Regarding the results of Moze model [17], a good accordance with the experimental values  $F(u_{s,max})$  and the design values is observed for the E1-1.5 et E1-2. However, the prediction overestimates the strength of specimens E2-1.5 and E2-2. It would be interesting to compare this model to other experimental tests with various geometries in order to confirm this observation concerning long slotted holes.

Regarding to the specimens E1-1 and E2-1, the model of Wald, comparing  $F_{pl}$  with  $F_{b,Rd,Wald}$ , on one hand and the model of Moze, comparing  $F(u_{s,max})$  and  $F_{b,Rd,Moze}$ , on the other hand present a high negative difference. This indicates that the analytical strength values are higher than the experimental ones. This observation shows that those analytical models are not suitable to describe the bearing behavior of those specimens. This conclusion was expected as the geometries of specimens E1-1 and E2-1 are out of the geometrical specifications of the models. Therefore, the analytical model needs to be adapted to predict the strength for geometries out of the standard recommendations, especially for small end-distance.

In order to observe the possibilities of adaptations of the model, the following section is dedicated to the analysis of the failure modes and the behavior of all specimens.

### 3.4. Failure modes

Figure 6 presents the failure modes of the specimens E1-1, E1-1.5, E1-2, E2-1, E2-1.5. The specimen E2-2 did not reach the failure because of the large bolt bending. However, the plastic behavior was reached (see figure 7).



(a) E1-1 (Tensions and shearing)



(b) E1-1.5 (Shearing and bearing)



(c) E1-2 (Shearing and bearing)



(d) E2-1 (Tensions and shearing)



(e) E2-1.5 (Shearing and bearing)

Figure 6: Failure modes observed on the specimens with large hole deformations

The observation of the failure modes shows two types of failure. The first one concerns the specimens E1-1.5, E1-2, E2-1.5 which present a dominant mode of bearing before failure. The bearing of the bolt in the hole is clearly visible. Furthermore, shearing failure of the plate is observed under the

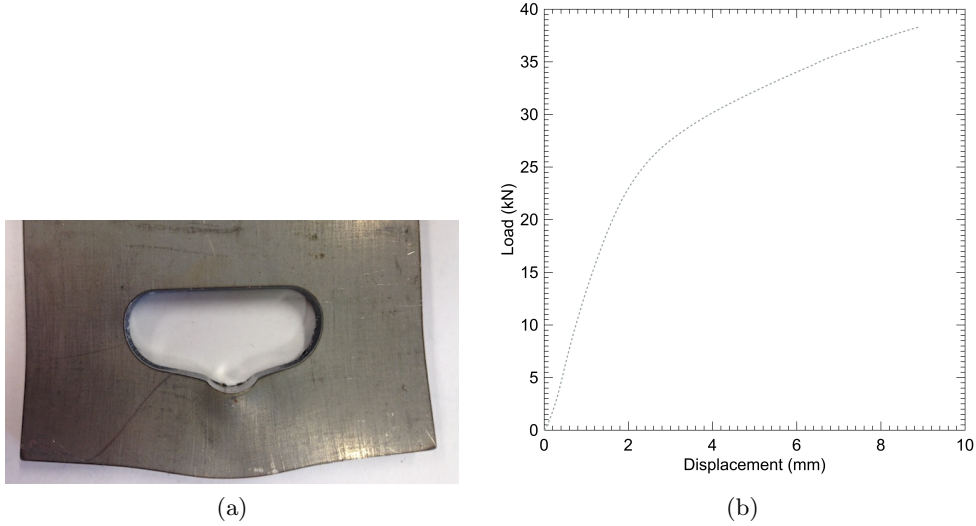


Figure 7: Specimen E2-2 after test and load-displacement curve

bolt. This failure mode is the one predicted by the model of the Eurocode NF-EN-1993-1-8 [18].

The second failure mode corresponds to a failure by tension and shear. Figure 6a and 6d present this failure for specimens E1-1 and E2-1. These two specimens present similar position of the crack section. Moreover, contrary to the failure of E1-1.5, E1-2, E2-1.5 which present a large penetration of the bolt in the zone under the bolt and so a reduction of the end-distance in this zone, for E1-1 and E2-1, the end-distance of the zone under the bolt remains similar to the one before test. This indicates a limited penetration of the bolt for E1-1 and E2-1 during tests. Only reduction of section is visible in the zone of the crack (necking) which indicates high tensile stresses at the failure due to the large deformation of the end-distance.

This observation can explain the negative difference observed in the table 6 between  $F_{pl}$  and  $F_{b,Rd,Wald}$  and in the table 7 between  $F(u_{s,max})$  and  $F_{b,Rd,Moze}$ . Indeed, these specimens seem to present a failure mode different

from that covered by the standard. The observation of two different failure modes is confirmed by the local analysis of strains using full field measurement. In the next sections, experimental results for specimens E1-1, E1-1.5 and E1-2 are presented in detail.

#### *3.4.1. Behavior of E1-1.5 and E1-2 specimens*

The load-displacement curve of specimen E1-2 is given in figure 8a with the positions of the loads illustrated by deformed shapes of specimen (Figure 10b to 10d). The main phenomenon observed during the test is the penetration of the bolt in the plate (Figure 8c). This phenomenon is accentuated for higher level of loading until failure. This specimen presents a bearing failure with a shearing fracture at final stage as shown in Figure 8d.

The specimen E1-1.5 with lower end-distance presents the same failure mode as specimen E1-2. The load-displacement curve of specimen E1-1.5 is shown on Figure 9a with the two loads (P1 and ultimate). The deformed shapes of the specimen observed during the test are shown on Figure 9b for the load corresponding to P1 and on Figure 9c for the ultimate load.

Two types of phenomena can be observed. The first one is the bending of the end-distance under bolt loading (see Figure 9b). This phenomenon corresponds to the slope change on the load-displacement curve (figure 9a). The second phenomenon is the bearing of the bolt on the end-distance zone. The bearing becomes predominant compared to the bending of the end-distance with the increase of the loading until shear failure.

#### *3.4.2. Behavior of specimen E1-1*

Figure 10a presents the load-displacement curve of specimen E1-1. This specimen has the same hole length as specimens E1-1.5 and E1-2, but its end-distance ( $e_3 = 1. d_0$ ) is smaller.

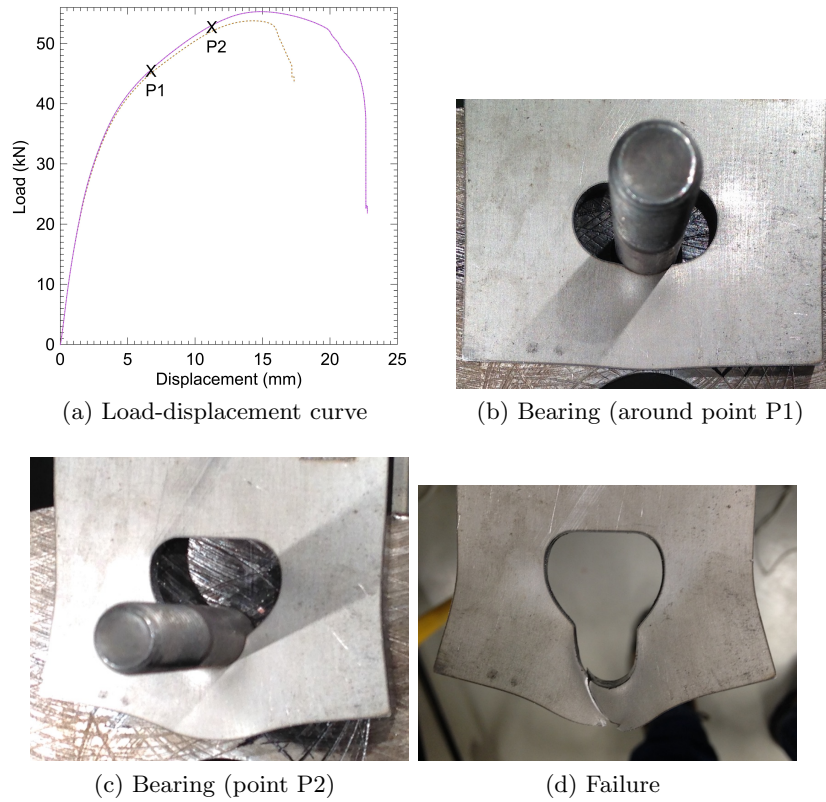
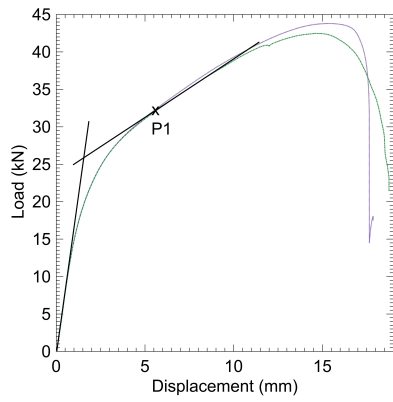


Figure 8: Experimental observations for the specimen E1-2

It can be observed in Figure 10b, corresponding to point P1 in the load-displacement curve in Figure 10a, that the bending of the steel part under the bolt is dominant in comparison to bearing. Large bending displacements are visible in figure 10c corresponding to point P2 in the load-displacement curve in Figure 10a. It induces a tension force in the end-distance and the failure. Indeed, a reduction of section (necking) is visible at the critical section (Figure 10d).

The length of the slotted hole is not directly considered in the analytical formula of current design rules to evaluate the strength. However, the experimental results point out the influence of the hole length on the strength values of bolted cover-plate with slotted holes. Besides, two main failure



(a) Load-displacement curve



(b) Deformation (Around point P1)



(c) Failure by shear and bearing

Figure 9: Experimental observations for the specimen E1-1.5

modes were observed: bearing or bending combined with tension at high load level. The next part presents an analysis of strain maps around the hole using full field measurement method. Two specimens with different failure modes have been chosen for this local analysis (specimens E1-1 and E1-1.5).

#### 4. DIC analysis of the local behavior of E1-1 and E1-1.5 specimens

In this section, analysis is focused on strain maps obtained for different loading levels for two end-plate dimensions  $e_3$  ( $13\text{ mm}$  for specimen E1-1 and  $19.5\text{ mm}$  for specimen E1-1.5). The aim is to illustrate the deformation mechanisms under the slotted hole. For that purpose, various strain maps,

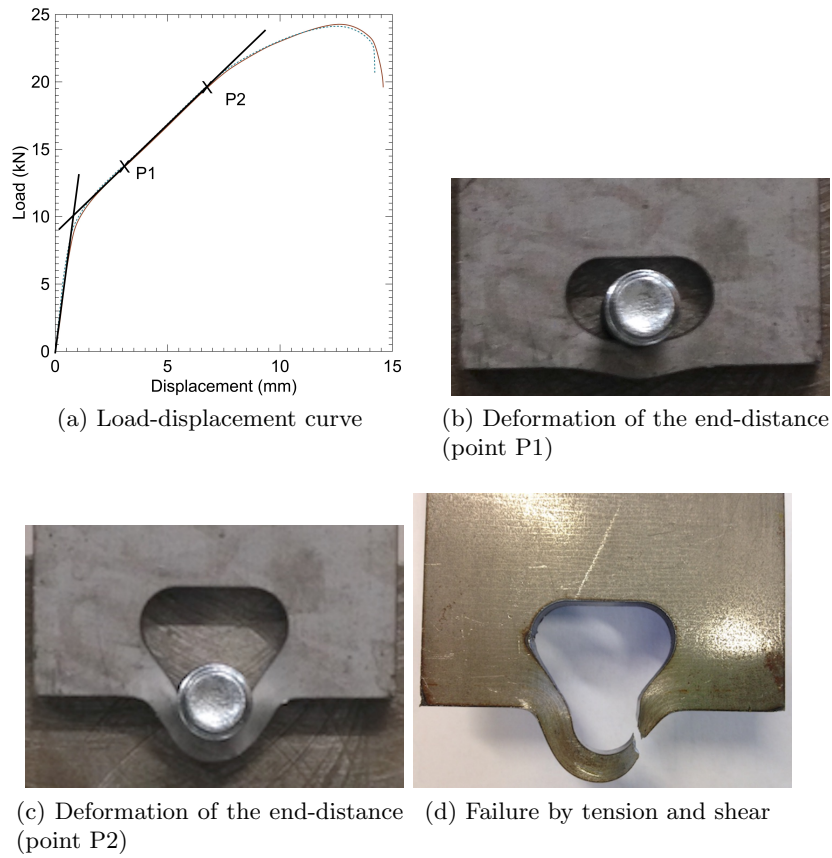


Figure 10: Experimental observations for the specimen E1-1

namely  $\varepsilon_{xx}$ ,  $\varepsilon_{yy}$ ,  $\varepsilon_{xy}$ ,  $\varepsilon_1$ ,  $\varepsilon_2$  are presented and analyzed for three loading levels : in the first linear phasis, at the changing of slope and in the second linear phasis (see Figure 15a for example).  $\varepsilon_{xx}$ ,  $\varepsilon_{yy}$  and  $\varepsilon_{xy}$  strain maps correspond to the strains in plane (x,y).  $\varepsilon_1$  and  $\varepsilon_2$  strain maps correspond to the major and minor principal strain maps.

#### 4.1. Tests set-up

All specimens were tested using a  $\pm 200$  kN Zwick testing machine. The displacement controlled tensile tests were realized with a displacement rate of the cross-head machine chosen equal to  $0.04$  mm/s. The two configura-

tions (E1-1 and E1-1.5) were equipped with full field measurement in order to determine the strain fields in the loaded zone at the end-distance of the specimens. For these specimens, the load-displacement curves were obtained using LVDT displacement sensors fixed on the plate using adapted support. The test set-up is presented in Figure 11.

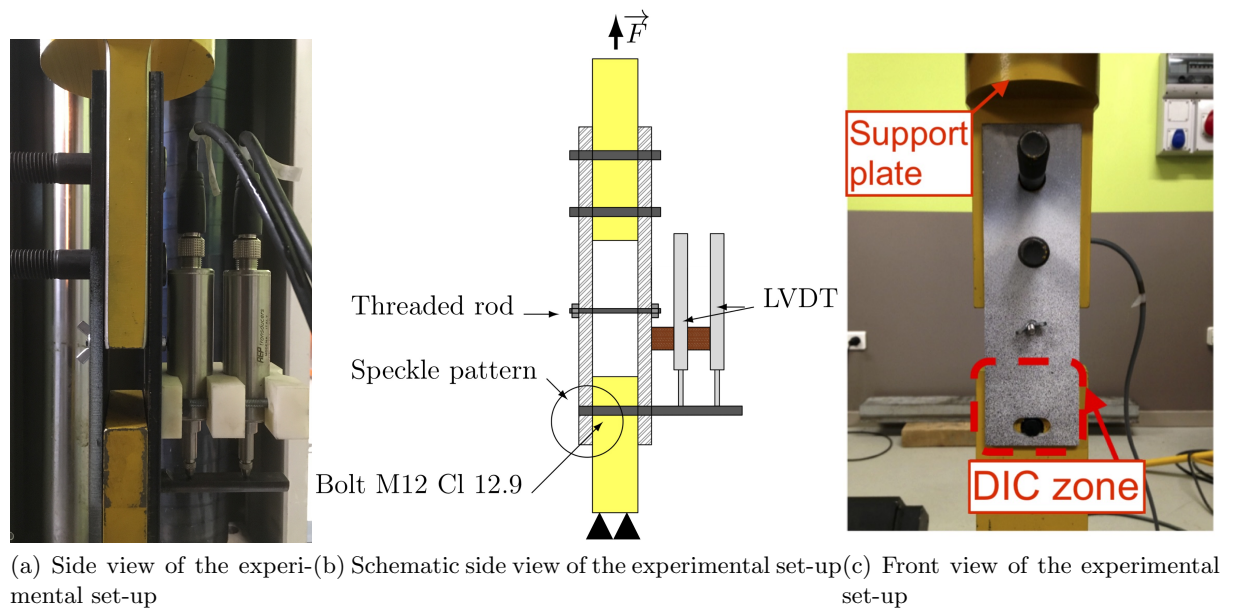
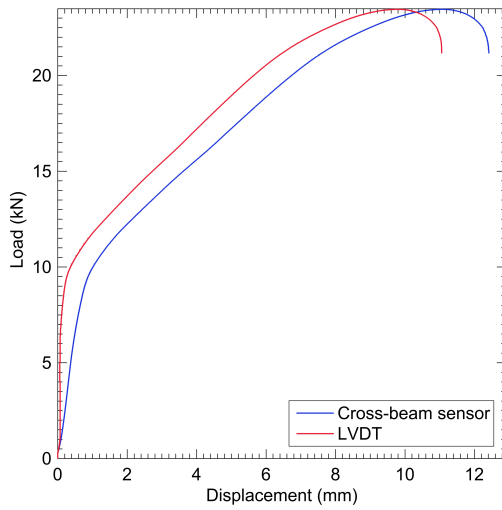


Figure 11: Test set-up (with DIC set-up)

#### 4.1.1. Displacement measurement for specimens E1-1 and E1-1.5

The two LVDT sensors measure the displacement along the bolt length so as to obtain the relative displacement between the bolt and the plate on a limited zone of the connection (see Figure 12b). The use of two sensors along the bolt gives the possibility to evaluate the part of relative displacement due to the bending of the bolt. Figure 12a presents, as example, the comparison of load-displacement curves obtained with the global displacement of cross-head machine and that obtained from LVDT sensor corrected by the rotation



(a) Example of a load-displacement curve with LVDT or cross beam sensor

(b) Bending of the bolt

Figure 12: Influence of displacement measurement

of the bolt.

#### 4.1.2. Image measurement

A PCO EDGE camera featuring a 14 bits/2048 x 2048 pixel CCD sensor and equipped with a 105 mm lens was used to capture images of the speckle. Full field measurements were used to measure the heterogeneous strain fields around the slotted hole. As the strain distribution is very important for the mechanical analysis and may significantly vary around the hole, it appears difficult to obtain rich results using standard strain gauges. Thus, it has been chosen to use a full field measurement technique which is well adapted for the observation of complex strain fields.

The acquisition frequency of the camera was chosen equal to  $0.91 \text{ images/s}$ . During the tests, the surface was illuminated using a cold light source to obtain a quasi-uniform lighting of the speckle. Figure 13 presents an overview of the experimental set-up.

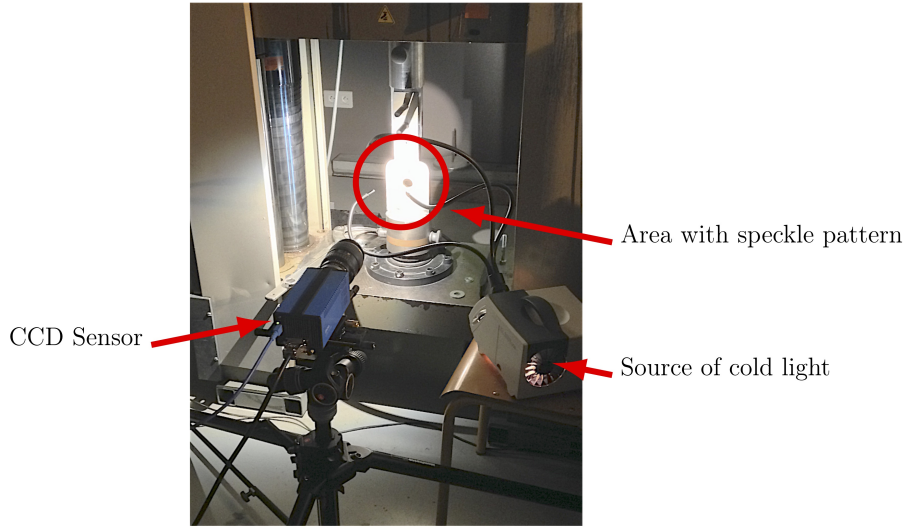


Figure 13: Camera measurement setup

The surface preparation consists in depositing a black speckle on a thin film of white paint sprayed on the surface of the studied zone localized around the slotted hole. The speckle size may influence the metrological performances of the technique, as detailed in [20]. That is why a special attention was paid on the speckle size in the present study. Figure 14a presents an example of the speckle pattern and its corresponding grey level histogram in Figure 14b.

In the present study, an open source 2D Digital Image Correlation MATLAB program Ncorr software [21] was used. Images were processed to deduce displacement and strain fields from the speckle images. The values of the parameters used for DIC analysis were: Subset size ( $SS$ ) = 10 *pixels*, Step Size ( $ST$ ) = 5 *pixels* and Strain Window ( $SW$ ) = 1 *pixel*, which represent standard settings for DIC. An estimate of the spatial resolution, which reflects the ability of the measuring technique to distinguish independent features in any strain map, can be calculated from these parameters by using the definition proposed in [22]:  $SP = (SW - 1) \cdot ST + SS$ . In the present

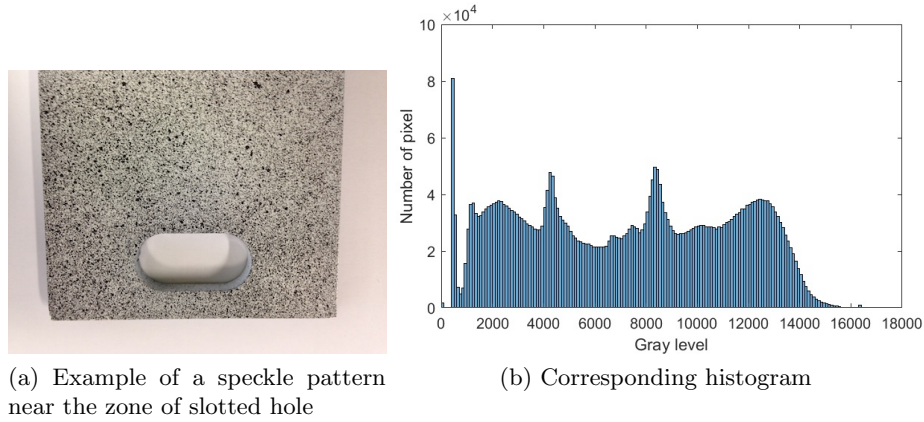


Figure 14: Example of speckle pattern

case, the spacial resolution is equal to  $SP = 10 \text{ pixels}$ .

Another metrological characteristic has to be considered: the resolution. It represents the lowest numerical values that can be measured by the DIC process out of the noise measurement. The resolution in displacement and the resolution in strain can be estimated by the standard deviation of the distribution of each quantity without any movement of the specimen tested. For each specimen, twenty speckle images have been stored without any movement, allowing for the calculation of the empirical standard deviations of the displacement and the strain maps. The obtained results are similar for both the horizontal ( $u_x$ ) and the vertical displacement ( $u_y$ ) fields on the one hand, and for the three  $\varepsilon_{xx}$ ,  $\varepsilon_{yy}$ ,  $\varepsilon_{xy}$  strain maps on the other hand. The average resolution in displacement was equal to  $4.6 \times 10^{-2}$  pixels, corresponding to  $1,6 \mu m$  and the average resolution in strain was equal to  $2. \times 10^{-3}$ .

#### 4.2. Material specifications

Table 8 summarizes the mechanical characteristics of the steel plates obtained from tensile coupon tests.

Specimen	$f_y$ (MPa)	$f_u$ (MPa)
E1-1	374	473
E1-1.5	290	380

Table 8: Mechanical characteristics of steel

M12 bolts with grade 12.9 are used in this part of the study. The aim is to avoid the failure mode of bolts in shear as the study is focused on the bearing failure mode of the connected plates. To obtain the real characteristics of the bolts, tests in tension were performed. The real value of bolt tensile strength is equal to 1530 MPa. To allow the observation of the strains on whole zone around the hole by DIC technique, the grade 12.9 is selected to limit the plastic deformations of the bolts during tests and the bolt head was sawn.

#### 4.3. Specimen E1-1

Figure 15 presents the global load-displacement curve and the corresponding  $\varepsilon_{xx}$ ,  $\varepsilon_{yy}$ ,  $\varepsilon_{xy}$ ,  $\varepsilon_1$ ,  $\varepsilon_2$  strain maps for three loading levels (7.4 kN, 12.0 kN and 17.7 kN), respectively. Those three load levels have been chosen to study the strain distribution before and after reaching the plastic strength  $F_{pl}$  which corresponds to the change of slope in the load-displacement curve. The corresponding  $\varepsilon_{xx}$ ,  $\varepsilon_{yy}$ ,  $\varepsilon_{xy}$ ,  $\varepsilon_1$ ,  $\varepsilon_2$  strain maps are presented in Figures 15c, 15f, 15i, 15l, 15o, for a loading level of 7.4 kN. Figures 15d, 15g, 15j, 15m, 15p for a loading level of 12.0 kN and in Figures 15e, 15h, 15k, 15n, 15q for a loading level of 17.7 kN, respectively. The principal strain maps  $\varepsilon_1$ ,  $\varepsilon_2$  shows two informations. On these figures are superimposed the orientation of the principal strain directions on the strain maps. The length of these lines is proportional to the value of the strain. An amplification on the length of the lines is applied in order to facilitate the exploitation. For

each level of load, the same amplitude is applied to the lines representing  $\varepsilon_1$  and  $\varepsilon_2$ .

For a loading of 7.4 kN, Figures 15c and 15f underline the bearing of the bolt in the end-distance area (see point A in these figures). Indeed, the  $\varepsilon_{xx}$  (Figure 15c) strain map shows two blue lobes on both sides of a red one. This type of deformation highlights the plastic flow of steel under the bolt and the two flattening areas of the steel. The  $\varepsilon_{yy}$  strain map (see Figure 15f) confirms this phenomenon. The blue zone under the contact between the bolt and the plate (point A) also shows the flattening of the end-distance due to the penetration of the bolt. This phenomenon of penetration of bolt can also be observed in Figure 15i with very localized shear strains around the contact area between the bolt and the plate. The principal strain maps presented in Figure 15l and 15o show that the strains are concentrated in the zone of penetration especially  $\varepsilon_2$  values. These results underline the fact that the penetration of the bolt is predominant at this stage of loading.

Figure 15d presents the  $\varepsilon_{xx}$  strain map corresponding to a global behavior intermediate between elasticity and plasticity (see blue circle in Figure 15a corresponding to 12.0 kN). This figure presents a red triangular zone under the bolt contact point (between points A and B). In order to analyse this phenomenon, Figure 16 presents the strain values along line AB for two loading levels equal to 7.4 kN and 12.0 kN, respectively. This strain distribution shows the development of a plastic flow in the x-direction near point B, with high strain level (0.032 for 12.0 kN, compared to 0.006 for 7.4 kN). The strain levels corresponding to the elastic limit of strain of this steel  $\varepsilon_e$

is calculated as  $\varepsilon_e = \frac{f_y}{E} = 1.8 \cdot 10^{-3}$  (E is the Young's modulus and  $f_y$  the yield strength equal to 374 MPa). The strain level is higher than  $\varepsilon_e$  for almost all points located along line AB. This observation allows to conclude

that around point A, the penetration of the bolt generate a plastification of the material. In the same time, for a load level equal to 12 kN, the slope of the strain curve from the middle of the line AB to point B illustrates the development of a plastic zone inducing a roation of the section arround line AB. For an analytical point of view, a plastic zone causes a transition from a behavior with small deformations to a large one. However, due to the hardening of steel, this plastic zone presents an increase of strength, which explains the increase of the load-displacement curve after the changing of slope. Moreover, the shearing of the end distance area (see Figure 15j) starts to develop along the end-distance. This phenomenon is more visible in Figure 15m and 15p that present the principal strains maps  $\varepsilon_1$  and  $\varepsilon_2$ . They present a slope at 45 degrees with the horizontal and vertical directions, respectively. The black dashes reflecting the two principal deformations present the same length for all points with a strain level higher at the middle of the hole than its border. This behavior is close to the one of a three-point bending beam. Finally, this phenomenon explains the changing of slope observed in the load-displacement curve.

The last analysis is dedicated to a loading equal to 17.7 kN, and corresponds to the global plastic behavior. Figure 15e shows the development of a plastic hinge that can be observed at the border of the hole. Indeed, the red zone around point C and the blue one around point D confirm this phenomenon with high positive strains (tension) in C and high negative strains (compression) in D. To illustrate this mechanical behavior, Figure 17 presents the  $\varepsilon_{xx}$  strain values along line CD for four different loading levels 7.4 kN, 12.2 kN, 15.0 kN, and 17.7 kN, respectively. The development of the plastic hinge progressively appears, resulting in an increase of the absolute value of the  $\varepsilon_{xx}$  strain values at points C and D with the loading

values. The development of the plastic hinge appears just after the slope change on the global load-displacement curve. Indeed, no significant strain is visible for 7.4 *kN*. For a loading of 12.2 *kN*, a positive strain value equal to  $7 \cdot 10^{-3}$  can be observed at point C. This value of strain corresponds to the beginning of strain hardening. For a loading of 15 *kN*, the plastic hinge is fully developed. This phenomenon induces an increase of the displacement visible in the global load-displacement curve after the slope change. Finally, the curve corresponding to a load of 17.7 *kN* confirms this phenomenon because all along the line CD, the deformations are higher than the elastic limit of deformation  $\varepsilon_e$  calculated as  $\varepsilon_e = \frac{f_y}{E} = 1.8 \cdot 10^{-3}$  (E is the Young modulus).

This behavior is typical of a beam in bending with three plastic hinges, two at the edges and one at the midspan of the end-distance. To complete the analysis, Figure 18 presents the  $\varepsilon_{xx}$  strain values along line (EF) versus load. It can be seen in this figure that below a load value of 15.0 *kN*, the strain values are very small (under 0.002). Beyond this value, the strain values rapidly increase. This increase of both strains and strain rates underlines the development of a tensile zone along the line (EF). To confirm the experimental observation leading to a tension failure, the orientation of the principal strains are calculated and presented in Figure 19. Figures 19a and 19b present  $\varepsilon_1$  and  $\varepsilon_2$  strain maps on which the principal strain orientations have been superimposed. The load value equal to 26.6 *kN* is close to the ultimate strength of the connection. The length of the cross-lines is proportional to the amplitude of the principal strains. The inclination of each cross is equal to the orientation of the principal directions of the strains. The length of lines representing  $\varepsilon_1$  is much higher than those representing  $\varepsilon_2$ .

#### 4.4. Specimen E1-1.5

In this section, the behavior of specimen E1-1.5 is analyzed similarly to the specimen E1-1.

Figure 20 presents the global load-displacement curve and the  $\varepsilon_{xx}$ ,  $\varepsilon_{yy}$ ,  $\varepsilon_{xy}$ ,  $\varepsilon_1$ ,  $\varepsilon_2$  strain maps for three loading levels (10.4 kN, 22.0 kN and 30.3 kN), respectively. The corresponding  $\varepsilon_{xx}$ ,  $\varepsilon_{yy}$ ,  $\varepsilon_{xy}$ ,  $\varepsilon_1$ ,  $\varepsilon_2$  strain maps are presented in Figures 20c, 20f, 20i, 20l, 20o for a loading level of 10.4 kN, in Figures 20d, 20g, 20j, 20m, 20p for a loading level of 22.0 kN and in Figures 20e, 20h, 20k, 20n, 20q for a loading level of 30.3 kN, respectively.

Both  $\varepsilon_{xx}$  and  $\varepsilon_{yy}$  strain maps corresponding to a loading level of 10.4 kN clearly underline that strains are localized under the bolt, the strain values for the other zones are very small. More particularly, the  $\varepsilon_{xx}$  strain map for 10.4 kN shows a red lobe (point A) with two blue ones on both sides of the red zone. This observation induces the same conclusion as for specimen E1-1, namely the penetration of the bolt in the end-distance area. This phenomenon is the first one that appears. The blue lobe (point A) visible in Figure 20f confirms this observation. The  $\varepsilon_{xy}$  map in Figure 20i shows the development of a shearing flow under the contact between the bolt and the plate (point A). The observation of the principal strains allows to confirm that the strains are only localized under the bolt contact zone.

Based on Figures 20d and 20g corresponding to a loading level equal to 22.0 kN, the global behavior intermediate between elasticity and plasticity is now analyzed. As for Specimen E1-1, the presence of a plastic section is visible, especially in zone (AB). Indeed, the development of the localized plastic section induces an increase of the elongation along the horizontal direction, which is visible along line (AB). The penetration of the bolt becomes predominant as it can be seen in the  $\varepsilon_{yy}$  strain maps with the large

blue lobe under point A. The  $\varepsilon_{xy}$  strains presented in Figure 20i confirm that the penetration of the bolt is predominant because of the presence of large lobes around point A. Moreover, the principal strains (Figures 20m and 20p) present directions of about 45 degrees around point A whereas they appear horizontal and vertical around point B. The strain level are equivalent for  $\varepsilon_1$  and  $\varepsilon_2$ . The strain levels are much higher around point A than around point B which underlines the fact that the penetration is predominant for this specimen.

Finally, the study of  $\varepsilon_{xx}$  and  $\varepsilon_{yy}$  (Figures 20e and 20h) for a loading level of 30.3 *kN* confirms the previous observations, that is the penetration of the bolt which characterize the behavior of specimen E1-1.5. The  $\varepsilon_{xy}$  map presented in Figure 20i proves that the maximum gradient of shearing is concentrated around line AB. The angle of the principal strains visible in Figure 20n and 20q confirm this observation. The behavior of this specimen is characterized by the bearing of the end-distance area. The phenomenon is followed by the development of another plastic hinge (Figure 20e) on the border of the hole but with a smaller amplitude than at the middle of the end-distance area. As the strain amplitudes are smaller compared to those observed along line (AB), this phenomenon has no effect on the failure mode, as observed in section 3.4.

To complete the analysis, Figure 21 presents the  $\varepsilon_{yy}$  strain values along line (AB) for three load levels: 10.4 *kN*, 22.0 *kN* and 30.3 *kN*. The influence of the bolt bearing on the  $\varepsilon_{yy}$  strain value is visible, especially around point A. The absolute  $\varepsilon_{yy}$  strain value increases from 0.001 et 0.08 for a load level increasing from 10.4 *kN* to 30.3 *kN*.

The analysis of the principal strains completes the study and validates the shear failure mode observed for that specimen. Figures 22a and 22b

present  $\varepsilon_1$  and  $\varepsilon_2$  strain maps on which the principal strain orientation have been superimposed. The load value, equal to  $39.4 \text{ kN}$ , is close to the ultimate strength of the connection. Due to speckle disbanding around point A where the bolt bearing creates a large plastic steel deformation, the principal strains at the border of the hole are not considered for this loading level. For all points where the principal strains are plotted, black lines corresponding to the principal strain values have quite the same length, especially in the circled zone presented in Figure 22. The angles of the principal directions is close to 45 degrees, reflecting a pure shear state. This is confirmed by the failure observed experimentally, which is clearly due to shearing and is consistent with the bearing mode.

#### *4.5. Overview*

The analysis presented in the two previous sections, concerning the behavior of the two specimens E1-1 and E1-1.5, shows a competition between two different aspects of the behavior in bolted cover-plate with slotted hole: the bending and the bearing of the end-distance area. Three plastic sections were observed for the specimens E1-1 and E1-1.5 a plastic zone under the bolt due to penetration and plastic hinges at the border of the hole due to bending of the end-distance. Concerning specimen E1-1, these plastic hinges induce large deformations in bending and lead to the development of tension due to second order effect, while specimen E1-1.5 at failure is mostly characterized by the bolt bearing on the end-distance area.

The analysis of bolted cover-plate with slotted holes allows to conclude that two phenomena are in competition : the bending of the end-distance and the bolt penetration. Both models of Wald and Moze predict the bearing failure. However, considering the bending of the end-distance could improve the bearing strength prediction.

## 5. Conclusion

This study of bolted cover-plate with slotted holes showed that during loading, two failure modes can arise in the end-distance zone under the bolt. The first one is characterized by a large bending of the end-distance that leads to an arch shape in tension. The second one is due to the bolt penetration (bearing) in the end-distance area. It has been shown that the length of the hole has an influence on the strength values of the connection. Using full field measurement technique for two specimens presenting two different failure modes (bending and bearing), it was observed that the bending of the end-distance zone and the bearing are in competition. Thus, the behavior is controlled by the ratio of stiffness of two components: the bending and the bearing of the end-distance area. Those observations lead to conclude that Wald model is adapted to geometries with a high predominance of the bearing mode. The length of the hole is not taken into account in this model. Besides, the design is very conservative for small and long slotted holes. The model of Moze presents a new way to design this type of connection considering the strength in the plastic phase of the behavior. Indeed, this model allows to take full advantage of the large deformation capacity of cover-plate with slotted holes. Moreover, it can be interesting to investigate the stiffness of this type of connection considering bending and bearing of the end-distance. This investigation could allow to predict the load-displacement curve of such connections to be used in the prediction of moment-rotation curve in more complex connections using this type of slotted-holes.

## References

- [1] A. Bouchair, J. Averseng, A. Abidelah, Analysis of the behaviour of stainless steel bolted connections, *Journal of Constructional Steel Research* 64 (11) (2008) 1264–1274. doi:10.1016/j.jcsr.2008.07.009.  
URL <http://linkinghub.elsevier.com/retrieve/pii/S0143974X08001685>
- [2] Y. Gong, Ultimate tensile deformation and strength capacities of bolted-angle connections, *Journal of Constructional Steel Research* 100 (2014) 50–59. doi:10.1016/j.jcsr.2014.04.029.  
URL <http://linkinghub.elsevier.com/retrieve/pii/S0143974X14001126>
- [3] A. Abidelah, A. Bouchair, D. Kerdal, Experimental and analytical behavior of bolted end-plate connections with or without stiffeners, *Journal of Constructional Steel Research* 76 (2012) 13–27. doi:10.1016/j.jcsr.2012.04.004.  
URL <http://linkinghub.elsevier.com/retrieve/pii/S0143974X1200096X>
- [4] Y.-F. Li, O. Jobe, C.-C. Yu, Y.-T. Chiu, Experiment and analysis of bolted GFRP beam-beam connections, *Composite Structures* 127 (2015) 480–493. doi:10.1016/j.compstruct.2015.03.001.  
URL <http://linkinghub.elsevier.com/retrieve/pii/S0263822315001713>
- [5] T. Dang Hoang, C. Herbelot, A. Imad, On failure mode analysis in a bolted single lap joint under tension-shearing, *Engineering Failure Analysis* 24 (2012) 9–25. doi:10.1016/j.engfailanal.2012.03.006.  
URL <http://linkinghub.elsevier.com/retrieve/pii/S1350630712000490>
- [6] A. Plumier, Behaviour of connections, *Journal of Constructional Steel Research* 29 (1-3) (1994) 95–119. doi:10.1016/0143-974X(94)90058-2.  
URL <http://linkinghub.elsevier.com/retrieve/pii/0143974X94900582>

- [7] T. Tajeuna, F. Legeron, P. Labossiere, M. Demers, S. Langlois, Effect of geometrical parameters of aluminum-to-steel bolted connections, *Engineering Structures* 102 (2015) 344–357. doi:10.1016/j.engstruct.2015.08.010.  
URL <http://linkinghub.elsevier.com/retrieve/pii/S014102961500509X>
- [8] L. Teh, M. Uz, Block shear failure planes of bolted connections â Direct experimental verifications, *Journal of Constructional Steel Research* 111 (2015) 70–74. doi:10.1016/j.jcsr.2015.04.006.  
URL <http://linkinghub.elsevier.com/retrieve/pii/S0143974X15001200>
- [9] B. Huns, G. Grondin, R. Driver, Tension and shear block failure of bolted gusset plates, *Canadian Journal of Civil Engineering* 33 (4) (2006) 395–408. doi:10.1139/105-104.  
URL <http://www.nrcresearchpress.com/doi/abs/10.1139/105-104>
- [10] E. Toussaint, S. Durif, A. Bouchair, M. Grediac, Strain measurements and analyses around the bolt holes of structural steel plate connections using full-field measurements, *Engineering Structures* 131 (2017) 148–162. doi:10.1016/j.engstruct.2016.11.033.  
URL <http://linkinghub.elsevier.com/retrieve/pii/S0141029616312640>
- [11] V. Karagiannis, C. Malaga-Chuquitaype, A. Elghazouli, Behaviour of hybrid timber beam-to-tubular steel column moment connections, *Engineering Structures* 131 (2017) 243–263. doi:10.1016/j.engstruct.2016.11.006.  
URL <http://linkinghub.elsevier.com/retrieve/pii/S0141029616311555>
- [12] S. Law, Z. Wu, S. Chan, Analytical model of a slotted bolted connection element and its behaviour under dynamic load, *Journal of Sound*

- and Vibration 292 (3-5) (2006) 777–787. doi:10.1016/j.jsv.2005.09.028.  
URL <http://linkinghub.elsevier.com/retrieve/pii/S0022460X05006668>
- [13] J. Butterworth, Ductile concentrically braced frames using slotted bolted joints, *Journal of the Structural Engineering Society New Zealand* 13 (1) (2000) 39–48.
- [14] Y. Araki, T. Endo, M. Iwata, Feasibility of improved slotted bolted connection for timber moment frames, *Journal of Wood Science* 57 (3) (2011) 247–253. doi:10.1007/s10086-010-1165-7.  
URL <http://link.springer.com/10.1007/s10086-010-1165-7>
- [15] F. Wald, V. Mazura, M. Moal, Z. Sokol, Experiments of bolted cover plate connections with slotted holes, Tech. rep., Czech Technical University, Prague, oCLC: 51190049 (2002).
- [16] F. Wald, Z. Sokol, M. Moal, V. Mazura, J.-P. Muzeau, Stiffness of cover plate connections with slotted holes, *Journal of Constructional Steel Research* 60 (3-5) (2004) 621–634. doi:10.1016/S0143-974X(03)00133-0.  
URL <http://linkinghub.elsevier.com/retrieve/pii/S0143974X03001330>
- [17] P. Moze, EN-1993-1-8:2005 (E)v. 2.1, draft (Mar. 2016).
- [18] CEN European Committee of standardization, NF-EN-1993. Eurocode 3-Design of steel structures, part 1.8. (2005).
- [19] W. Tizani, The Bearing Capacity of Plates Made with Long-slotted Bolt Holes:, Tech. rep. (Jan. 1999).
- [20] M. Bornert, F. Bremand, P. Doumalin, J.-C. Dupre, M. Fazzini, M. Grediac, F. Hild, S. Mistou, J. Molimard, J.-J. Orteu, L. Robert,

Y. Surrel, P. Vacher, B. Wattrisse, Assessment of Digital Image Correlation Measurement Errors: Methodology and Results, *Experimental Mechanics* 49 (3) (2009) 353–370. doi:10.1007/s11340-008-9204-7.  
URL <http://link.springer.com/10.1007/s11340-008-9204-7>

[21] J. Blaber, B. Adair, A. Antoniou, Ncorr: Open-Source 2d Digital Image Correlation Matlab Software, *Experimental Mechanics* 55 (6) (2015) 1105–1122. doi:10.1007/s11340-015-0009-1.  
URL <http://link.springer.com/10.1007/s11340-015-0009-1>

[22] P. Reu, Virtual strain gage size study, *Experimental Techniques* 39 (5) (2015) 1–3.

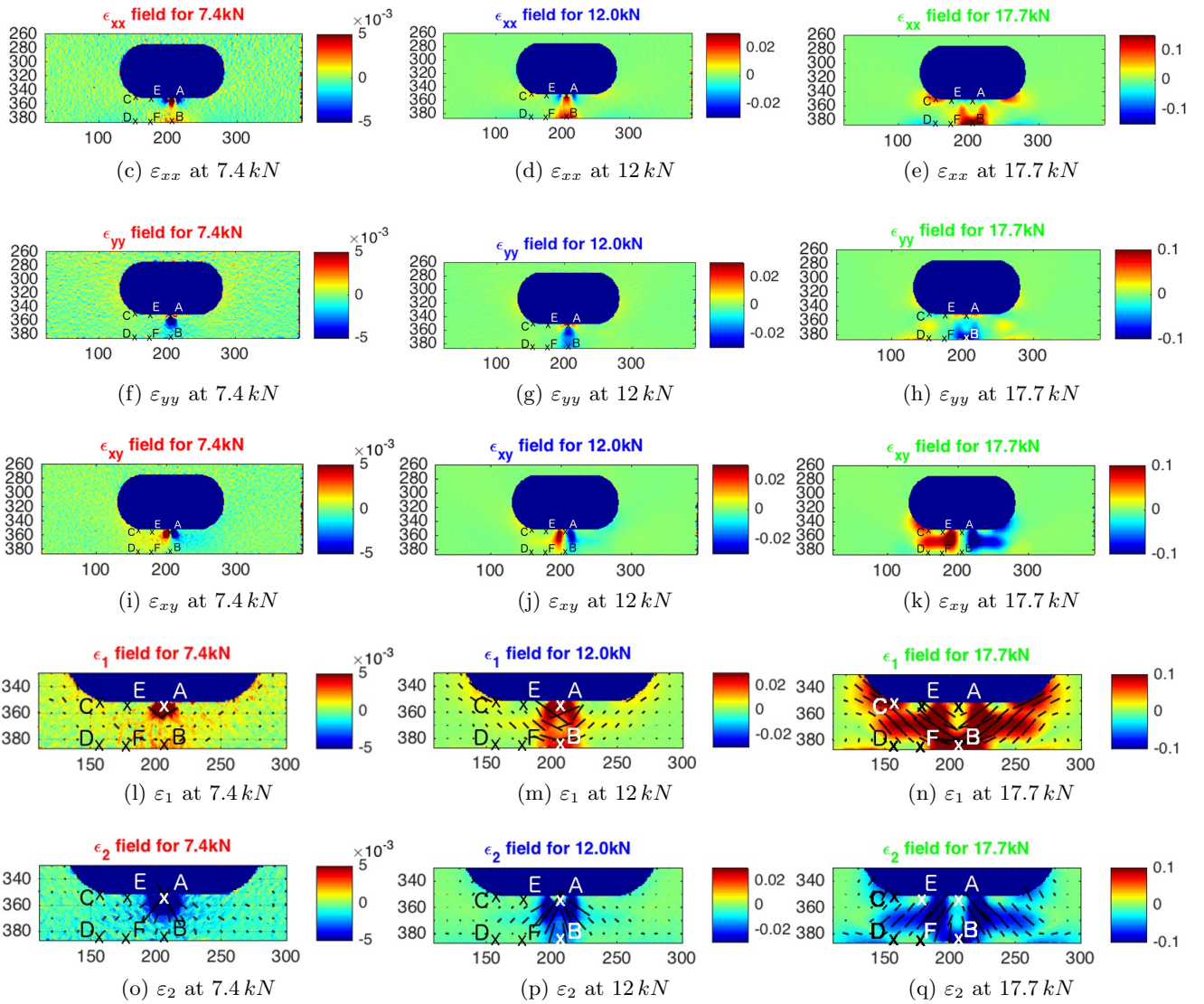
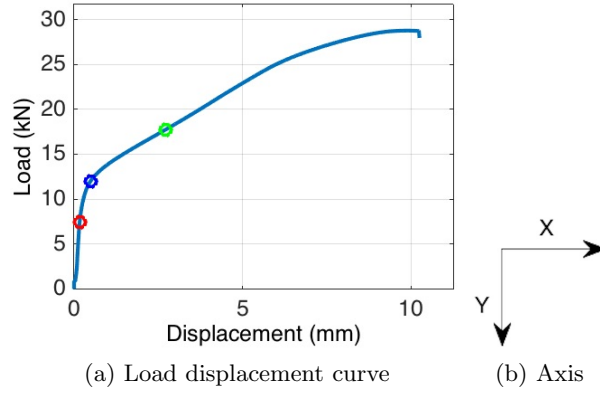


Figure 15: Strain map  $\epsilon_{xx}$ ,  $\epsilon_{yy}$ ,  $\epsilon_{xy}$ ,  $\epsilon_1$  and  $\epsilon_2$  at three loading levels for E1-1

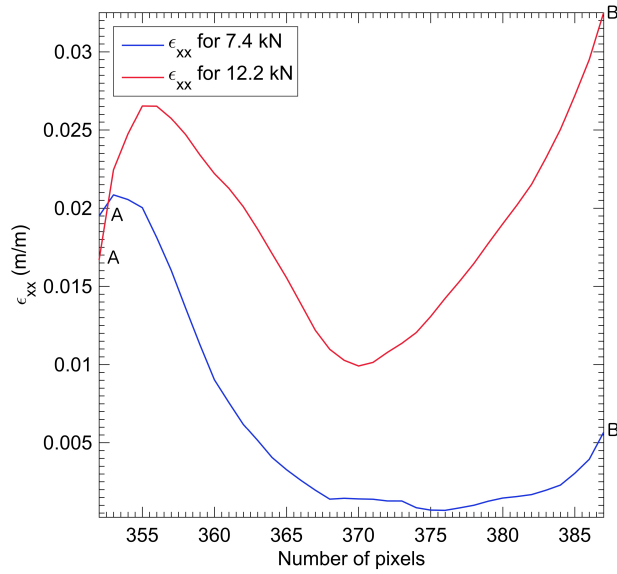


Figure 16:  $\epsilon_{xx}$  along the line AB depending on the loading

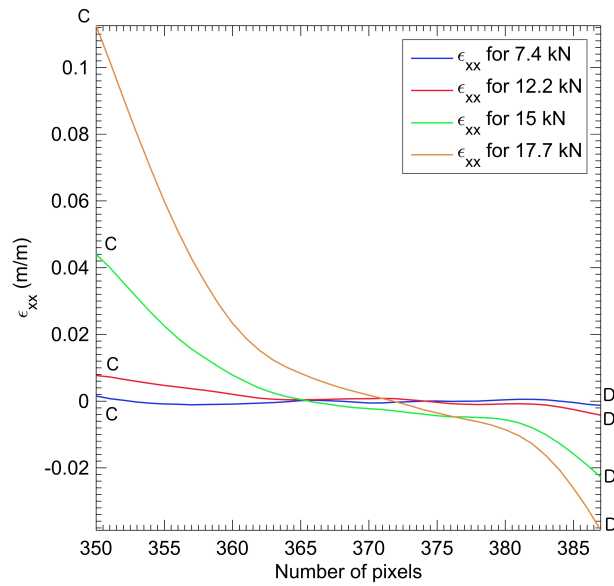


Figure 17:  $\epsilon_{xx}$  along the line CD depending on the loading

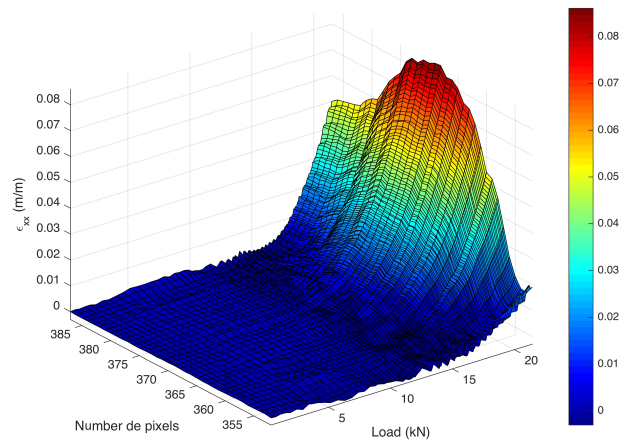


Figure 18:  $\varepsilon_{xx}$  along the line EF depending on the loading

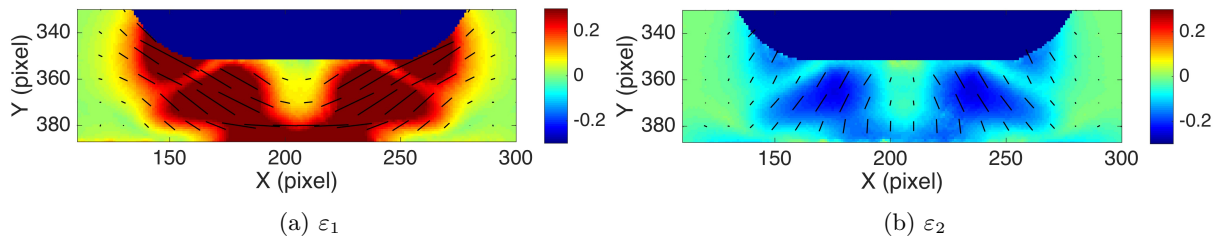
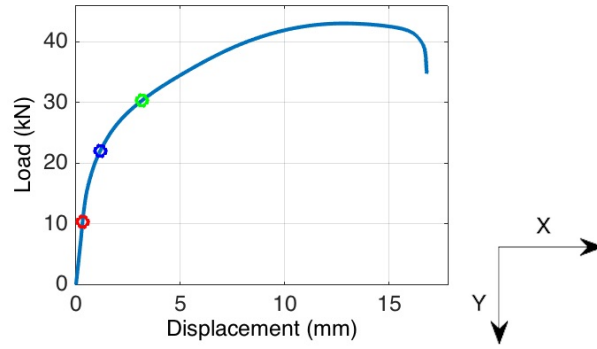


Figure 19: Principal deformations for E1-1 at 26.6 kN



(a) Load displacement curve

(b) Axis

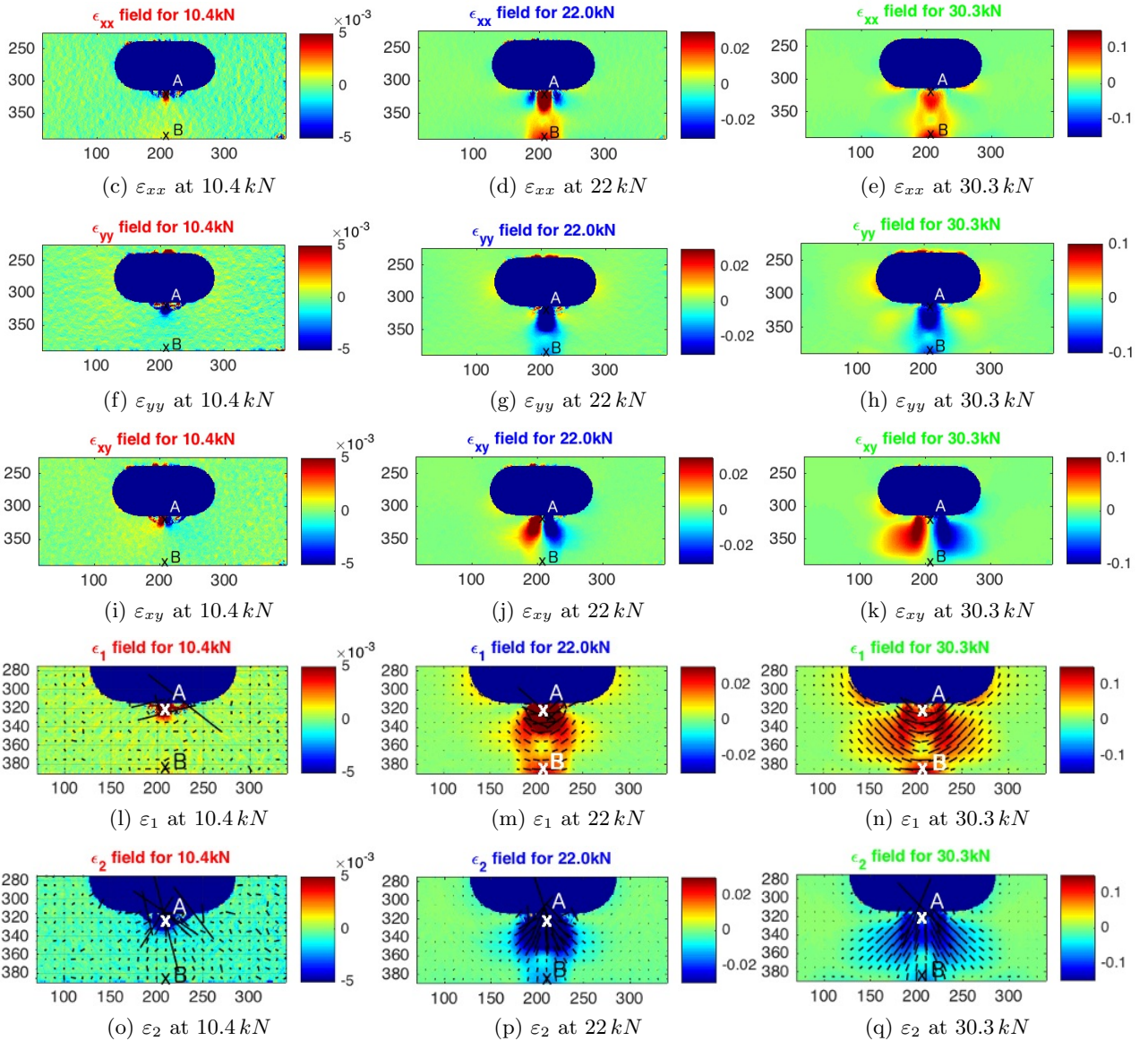


Figure 20: Strain map  $\epsilon_{xx}$ ,  $\epsilon_{yy}$ ,  $\epsilon_{xy}$ ,  $\epsilon_1$  and  $\epsilon_2$  at three loading levels for E1-1.5

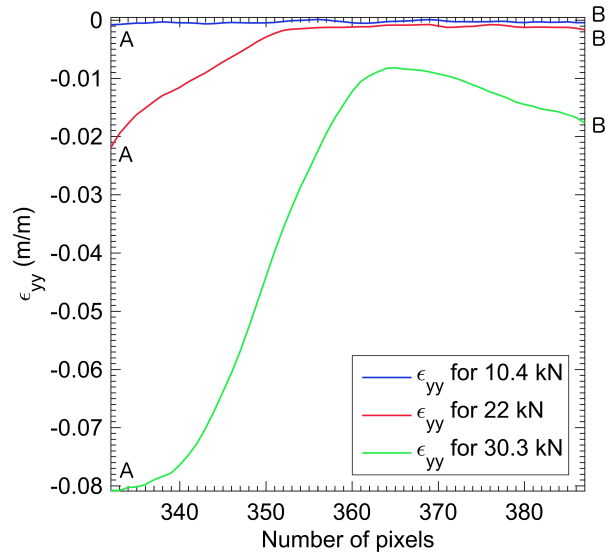


Figure 21:  $\epsilon_{yy}$  along the line AB at three loading levels

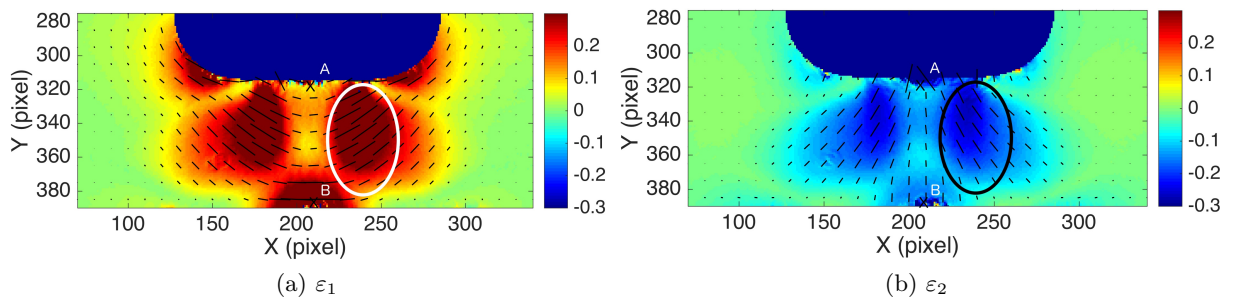


Figure 22: Principal deformations for E1-1.5 at 39.4 kN